Journal of Alloys and Compounds 851 (2021) 156931

Contents lists available at ScienceDirect

Journal of Alloys and Compounds

journal homepage: http://www.elsevier.com/locate/jalcom

Precipitation and aging phenomena in an ultrafine grained Al-Zn alloy by severe plastic deformation

Yonghao Zhao [a, *], Jizi Liu [a, **], Troy D. Topping [b], Enrique J. Lavernia [c]

[a] Nano and Heterogeneous Materials Center, School of Materials Science and Engineering, Nanjing University of Science and Technology, Nanjing, 210094, China
[b] Department of Mechanical Engineering, California State University, Sacramento, CA, USA
[c] Department of Materials Science and Engineering, University of California, Irvine, CA, 92697, USA

ARTICLE INFO

Article history:
Received 18 October 2019
Received in revised form
13 August 2020
Accepted 27 August 2020
Available online 31 August 2020

Keywords:
Ultrafine grained 7075 Al
Precipitation
Strength and ductility
Microstructures

ABSTRACT

The post-deformation aging response and underlying precipitation kinetics in ultrafine-grained, age-hardened alloys processed by severe plastic deformation are critical and heretofore poorly understood phenomena that ultimately influence mechanical behavior. In this study, a supersaturated solid solution 7075 Al alloy was processed by equal-channel-angular pressing (ECAP) route Bc at 250 °C for 6 passes to attain ultrafine grained (UFG) structures. Thermal and mechanical analyses revealed that there are three sequential phase transitions that govern post-deformation aging: first, dissolution reactions of Guinier-Preston (GP) zones, metastable η_p and η' precipitates which correspond to slight decreases in strength and ductility; second, afresh precipitating of GP zones, metastable η_p and η'/stable η phases corresponding to an increase in strength with significant decrease in ductility; and third, subsequent η transformation of the metastable η' and η_p as well as coarsening of stable η phases corresponding to a dramatic decreases in strength. Microstructural analysis suggests that the significant decrease in ductility may be attributed to grain boundary precipitation of the metastable η_p and η'/stable η phases.

1. Introduction

Energy considerations have prompted the study of high strength light-weight alloys for weight critical applications. Light-weight structural materials such as Al, Mg and Ti for example, are widely used in aerospace, transportation and biomedical industries, because when properly designed into engineering systems, these materials can lead to reductions in green house gases, such as CO_2. Recent results suggesting that it is possible to obtain significant (5–10 times) increases in the strength of bulk nanostructured (10–100 nm grain size, NS) and/or ultrafine grained (100–1000 nm grain size, UFG) Al, Mg and Ti alloys which have prompted numerous studies [1]. Despite encouraging early results, it is now apparent that these increases in strength are accompanied by poor ductility [2–8], low thermal stability [9,10] and high manufacturing costs, which have tempered engineering applications of these systems.

Severe plastic deformation (SPD) methods are widely used to generate NS and UFG microstructures by imposing high strains to induce dislocation generation and rearrangement into arrays of high-angle boundaries [11]. Amongst the various SPD techniques available, equal-channel angular pressing (ECAP) has been extensively applied to single-phase pure metals [12,13], such as Al [14–16], Cu [17–19] and their solid solution alloys [20–25]. Interestingly, however, inspection of the published literature shows that the number of reports on ECAP processed complex alloys, such as the age-hardened 7000 series of Al alloys where aging treatment and precipitation kinetics play dominant roles, are limited [26–51].

In the case of the 7000 Al series with different Zn:Mg ratios, the decomposition sequence is [52–55]:

Table 1
Chemical compositions of the as-received 7075 Al alloy analyzed in Luvak Inc. (Boylston, MA). The analysis method is direct current plasma emission spectroscopy – ASTME – 1097-03. The elements detected in excess of 0.01% were listed.

Elements	Zn	Mg	Cu	Fe	Si	Mg	Cr	Mn	Ti	Total others	Al
Wt.%	5.80	2.50	1.55	0.21	0.098	0.050	0.20	0.30	0.025	<0.15	balance

* Corresponding author.
** Corresponding author.
E-mail addresses: yhzhao@njust.edu.cn (Y. Zhao), jzliu@njust.edu.cn (J. Liu).

https://doi.org/10.1016/j.jallcom.2020.156931

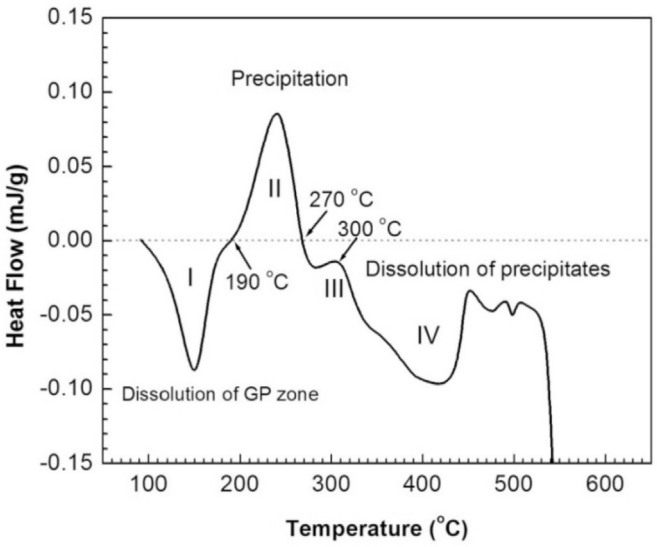

Fig. 1. DSC curve of the as-ECAPed UFG 7075 Al with a heating rate of 20 °C/min. The two endothermic reactions at lower temperature range of about 100–190 °C (as marked as region I in the figure) and higher temperature range higher than 270 °C (region IV) were resulted from the dissolutions of GP zones and precipitates, respectively. The two exothermic reactions at intermediate temperature ranges of 190–270 °C and 270–330 °C (Regions II and III, respectively) were due to precipitates.

Supersaturated Solid Solution (α_{SSS}) → $GP_{\eta'}$ zones → η' → η ($MgZn_2$), Zn/Mg < 2;

Supersaturated Solid Solution (α_{SSS}) → $GP_{\eta p}$ zones → η_p → η ($MgZn_2$), Zn/Mg > 2.

During aging, the supersaturated solid solution decomposes, first decomposed into GP II zones ($GP_{\eta'}$ or $GP_{\eta p}$), then to a metastable phase η' (coherent) or η_p (semi-coherent), and finally to the non-coherent equilibrium $MgZn_2$ (η) phase. There are two types of coherent GP zones: I and II [56–58]. GP II are zones consisting of a few atoms in thickness on {111}-Al planes formed from vacancy-rich solute clusters (VRC) [59]. The Z-contrast imaging revealed that there are two types of GP II zones: $GP_{\eta'}$ and $GP_{\eta p}$, depending on the atomic ratios of Zn/Mg [54,55]. $GP_{\eta p}$ is distinguished from $GP_{\eta'}$ by their characteristic thickness of 7 atomic-layer and structurally stable double-atomic-panel [54,55]. GP I zones are spherical with internal ordering on {100}-planes. The plate shaped η' and η_p are the main hardening precipitates and η' is characterized by a hexagonal structure (although an orthorhombic structure has also been reported [60]). In contrast, the η_p phase has a hexagonal lattice with parameters $a = 0.496$ nm and $c = 4d_{111Al} = 0.935$ nm (here d_{111Al} is distance of (111) plane of Al lattice), and finally transformed into the η phase. The stable η phase has a cylindrical morphology and consists of the hexagonal Laves phase [61]. Moreover, the η phase has been reported to nucleate from α_{SSS} at elevated temperatures [62].

In an early study it was reported that a 7000 series alloy

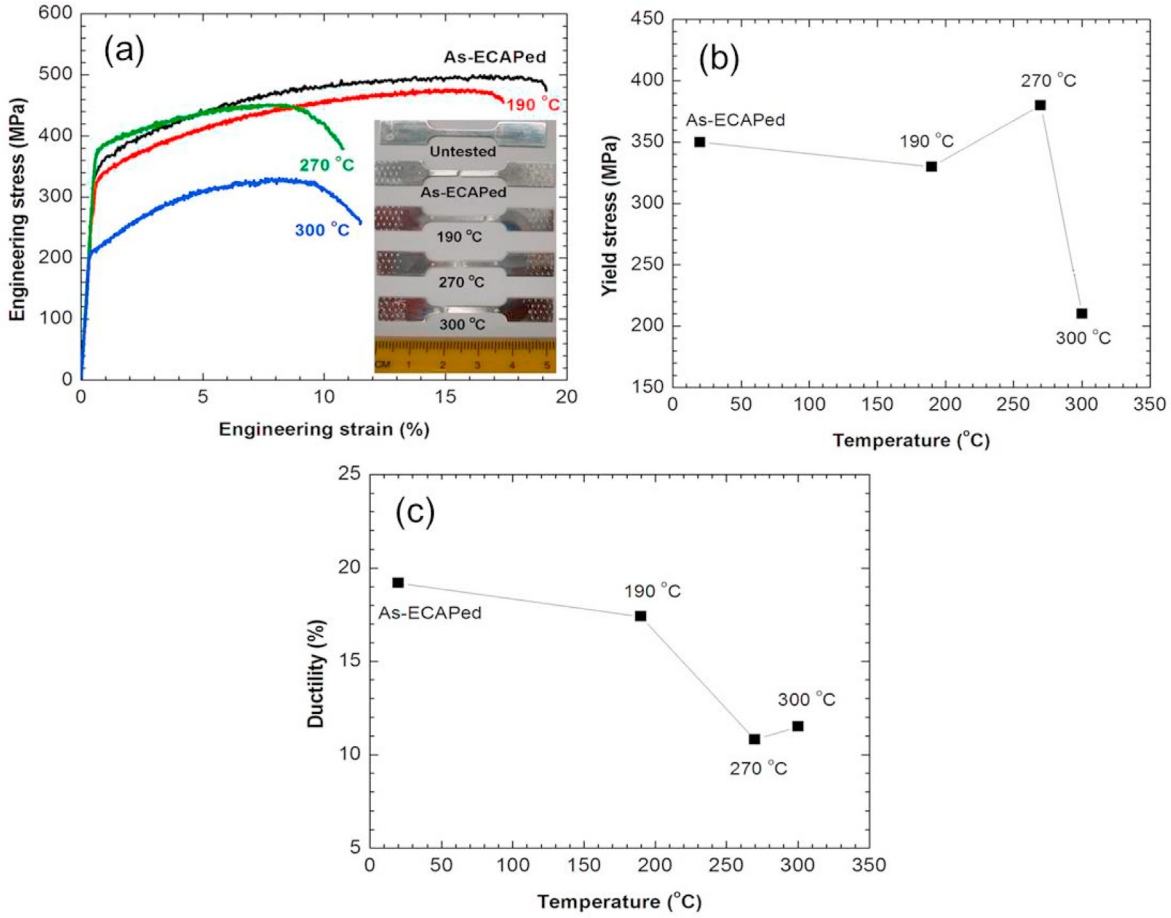

Fig. 2. (a) Tensile engineering stress-strain curves of the as-ECAPed 7075 Al and the samples heating up to 190, 270 and 300 °C with a heating rate of 20 °C/min. The inset shows the fractured tensile specimens with a dimension of 15 × 1 × 2 mm. (b,c) Heating temperature dependence of the yield strength (b) and ductility (c) of the UFG 7075 Al. The heating rate is 20 °C/min.

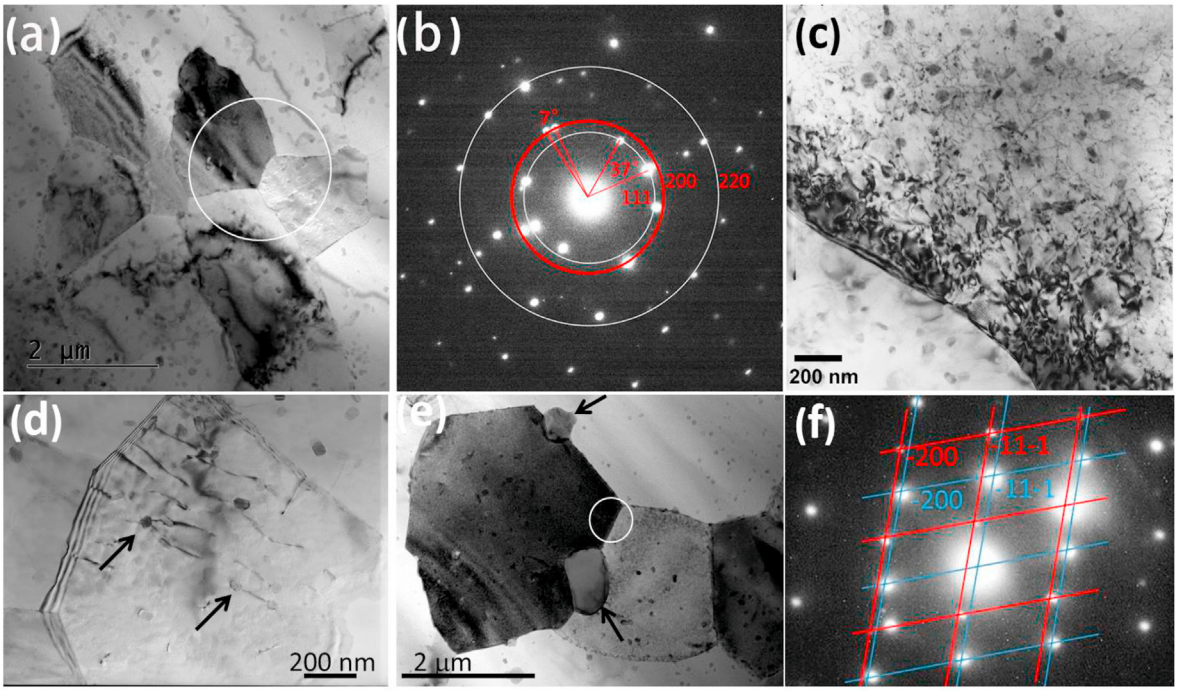

Fig. 3. (a) Bright-field TEM image of the as-ECAPed 7075 Al alloy showing equiaxed grains with spherical CrMn-rich particles. (b) Selected area electron diffraction (SAED) pattern of several grains marked by white circle in (a) revealing these grains have both high angle grain boundary of 37° and low angle grain boundary of 7°. (c) Large magnification TEM image showing a grain containing high-density dislocation networks mixed with precipitates. (d) Large magnification TEM image showing a grain containing low density of dislocations pinned by CrMn-rich phase, as indicated by the black arrows. (e) Bright field TEM image and (f) SAED pattern showing a small misorientation angle of 8° between the two circled grains. The blue and red lines were drawn to distinguish the two diffraction patterns from the two circled grains. Two recrystallized grains below 1 μm were pointed by black arrows. (For interpretation of the references to colour in this figure legend, the reader is referred to the Web version of this article.)

fractured, after only two ECAP passes, and this behavior was attributed to the hardening effect of GP zones and η′ phases [26]. In more recent work, it was reported that additional deformation strain (e.g., increase in the number of passes) could be imposed on the 7000 series of Al alloys by controlling room-temperature aging time (i.e., limiting GP zone formation) [30]. Another strategy that has emerged during efforts to facilitate severe plastic deformation of "difficult-to-work" Al alloys is to use elevated temperatures during ECAP [29,38]. The presence of elevated temperatures, however, limits control of recovery of the ultrafine grains and precipitation reactions. In related studies, post-deformation aging of ultrafine grained 7075 Al alloy has been shown to influence precipitation kinetics and hence the resultant mechanical behavior [26,27]. For example, ECAP, followed by room temperature aging, of 7075 Al led to an ultrafine grained microstructure and a yield strength of 700 MPa, albeit with limited ductility [26,27]. The high strength was rationalized on the basis of a high density of GP zones and dislocations. A two-step aging approach was then applied to the ECAPed 7075 to increase the density of nucleation sites for precipitates, effectively resulting in 10% ductility while retaining a strength value of 615 MPa [63]. The enhanced ductility was attributed to dislocation recovery during aging, whereas the high strength resulted from the precipitation of the metastable phase [63].

The above discussion suggests that published information on the mechanisms that govern the behavior of precipitation strengthened systems during severe plastic deformation processing is limited, and hence fundamental knowledge is lacking. Hence, the present work was undertaken in an effort to provide insight into the following two questions. What is the influence of elevated temperatures on the precipitation and structural phase transformations that occur during ECAP? Can this information be then used to attain combinations of strength and ductility in precipitation hardened UFG systems, such as 7075 Al?

2. Experimental materials and procedures

2.1. Sample preparation

Commercial 7075 Al alloy rods, with a diameter of 18 mm were treated at 480 °C for 5 h to form a homogeneous solid solution with an initial grain size of approximately 40 μm, and then quenched to room temperature in water. The chemical analysis indicates that the main alloying elements are Zn, Mg and Cu, as listed in Table 1.

The quenched 7075 Al alloy rods were immediately placed in an ECAP die, with a diameter of 18 mm and heated to 250 °C at a rate of ~20 °C/min. The ECAP die has an L-shape channel with an intersecting channel angle of 90° and an outer arc angle of 45°, which imposes an effective strain of approximately one per ECAP pass. The samples were processed for eight passes by route Bc in which the sample was rotated by 90° in the same direction between each pass in the procedure.

2.2. Room temperature tensile testing

Flat dog-bone tensile specimens with gauge dimensions of 15 × 1 × 2 mm were sectioned by electrical discharge machining (EDM) from the central regions of the UFG 7075 Al rods with a gauge axis parallel to the extrusion direction. All tensile specimens were finally polished using a diamond suspension with particle size of 25 nm. Three samples were prepared for each condition in order to ensure reproducibility of results. Uniaxial tensile tests were performed at room temperature on an Instron 8801 universal testing machine (UTM) using Bluehill 2 software with an initial

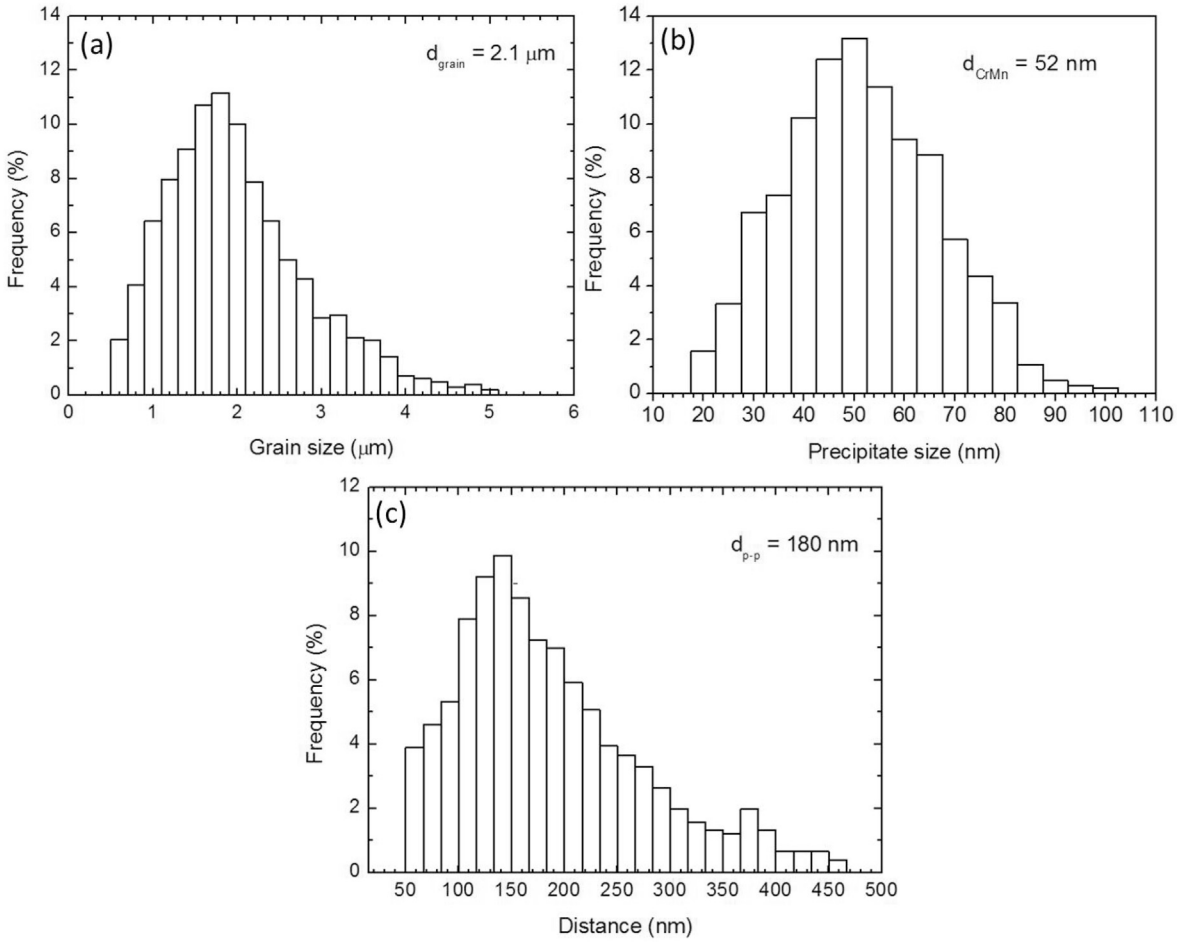

Fig. 4. Histograms of (a) grain size, (b) CrMn rich particle size and (c) CrMn rich particle interval in the as-ECAPed 7075 Al alloy. d_{grain}, d_{CrMn} and d_{p-p} represent their average values, respectively.

quasi-static strain rate of 10^{-3} s^{-1}. The strain was measured by using a standard non-contacting video extensometer with a 100 mm field-of-view lens.

2.3. Thermal analysis and treatment

Thermal analysis was performed in a PerkinElmer differential scanning calorimeter (DSC-7). Small rectangles sectioned from the ECAPed rods were polished for DSC measurements. The polished rectangles were sealed in Al pans and heated in a flowing Ar atmosphere at a constant heating rate of 20 °C/min; an additional empty Al pan was used as a reference. To determine mechanical properties and study microstructure evolution, some of the tensile specimens were heated to exothermic and endothermic peak-end temperatures (i.e., 190, 270 and 300 °C) at a heating rate of 20 °C/min in a protective Ar atmosphere, and then quenched to room temperature at a cooling rate of 500 °C/min. Three samples were prepared for each annealing condition in order to ensure reproducibility of results.

2.4. Microstructure characterization

The grip sections of the tensile specimens were examined using transmission electron microscopy (TEM). TEM specimens were prepared by first mechanically grinding the samples to a thickness of about 20–30 μm, then dimpling to a thickness of about 10 μm, and finally ion-milling to a thickness of electron transparency using a Gatan Precision Ion Milling System with an Ar + accelerating voltage of 4 kV and a temperature below 35 °C. TEM observations were conducted with a Philips CM12 microscope operated at 100 kV. An FEI Titan G^2 80–300 TEM, with an aberration-corrector implemented below its objective lens for imaging and an energy dispersive spectrometer (EDS) for component analysis, was employed to examine nano-sized precipitates and mapping. In its TEM mode, an information resolution of 0.07 nm can be reached at 300 kV. In its scanning TEM (STEM) mode, a point resolution of 0.16 nm was designed at 300 kV. Using high-angle annular dark-field (HAADF) detector, the image represents a Z-contrast proportional to $Z^{1.7\text{-}2.0}$ [64], where Z is the atomic numbers of the atoms in the specimen. Here, the HAADF-STEM images were performed with a half-angle of 21.4 mrad for probe convergence and a collection inner semi-angle of 53 mrad. The fracture surfaces were imaged by an FEI-XL30 SFEG scanning electron microscopy using a beam of 25 kV.

3. Experimental results and discussion

3.1. Thermal analysis

The DSC scanning curve of the as-ECAP processed 7075 Al alloy is shown in Fig. 1. It is apparent that the sample has an endothermic reaction that occurs in the lower temperature range from about 100

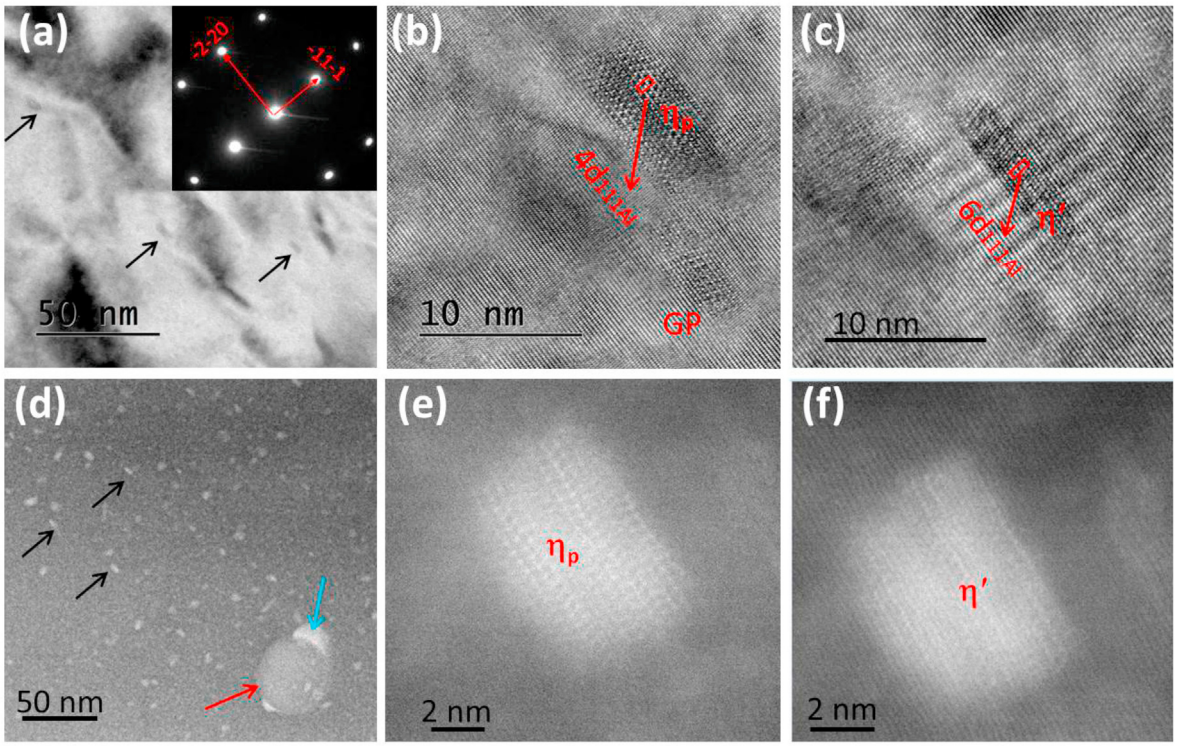

Fig. 5. The morphology and crystallography of precipitates in the as-ECAPed 7075 Al alloy viewed along a <112>$_{Al}$ direction. (a) Bright field TEM image of the precipitates pointed by black arrows and SAED pattern (inset). (b,c) HRTEM images of GP II zone, η_p, η', respectively. (d) The HAADF-STEM image of the precipitates pointed by black arrows, the CrMn rich particle was pointed by red arrow, and the Zn rich precipitates on the surface of CrMn rich particle was pointed by blue arrow. (e,f) High-magnification HAADF-STEM images of η_p and η' precipitates, respectively. (For interpretation of the references to colour in this figure legend, the reader is referred to the Web version of this article.)

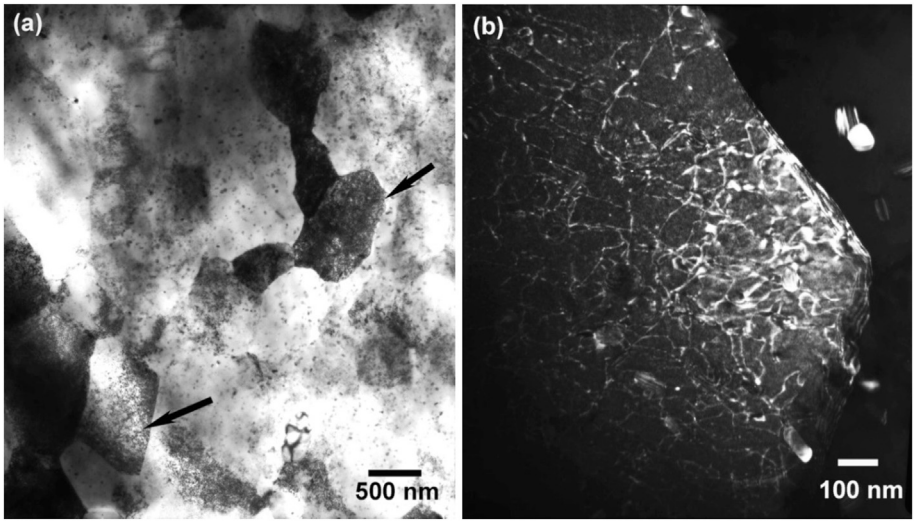

Fig. 6. (a) Bright-field TEM image of the UFG 7075 Al alloy heated up to 190 °C. Two grains containing a high density of dislocations are marked by arrows. (b) dark-field TEM image showing dislocation network pinned by precipitates.

to 190 °C (as marked as region I in the figure), two exothermic reactions at intermediate temperature ranges of 190–270 °C and 270–330 °C (regions II and III), and an endothermic reaction when temperature is higher than 270 °C (region IV). The 2nd exothermic peak is noted to overlap with the 2nd endothermic peak. On the basis of related literature data [65–68], the 1st and 2nd endotherms are attributable to the dissolution of the GP zones and the equilibrium hexagonal η phase, respectively. The intermediate exothermic regions include the formations of the metastable η' phase and the equilibrium η phase, as well as their coarsening. We will perform critical microstructural characterizations on these exothermic and endothermic reactions in section 3.3.

3.2. Tensile properties

The representative engineering stress-strain curves of the as-ECAPed 7075 Al alloy and the samples heated up to 190, 270 and 300 °C with a heating rate of 20 °C/min are compared in Fig. 2(a).

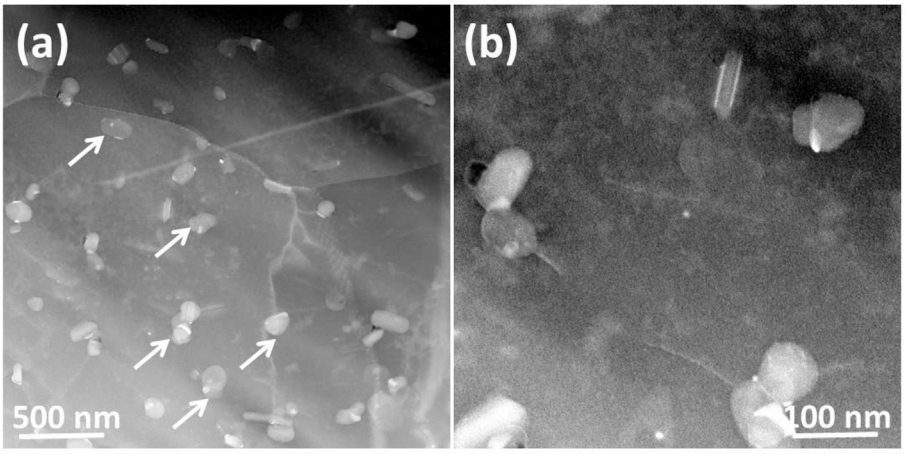

Fig. 7. The HAADF-STEM images of the ECAPed 7075 Al heated up to 190 °C viewed along a $<112>_{Al}$ direction. (a) CrMn rich phases were pointed by white arrows. (b) Magnified HAADF-STEM image of CrMn rich precipitate.

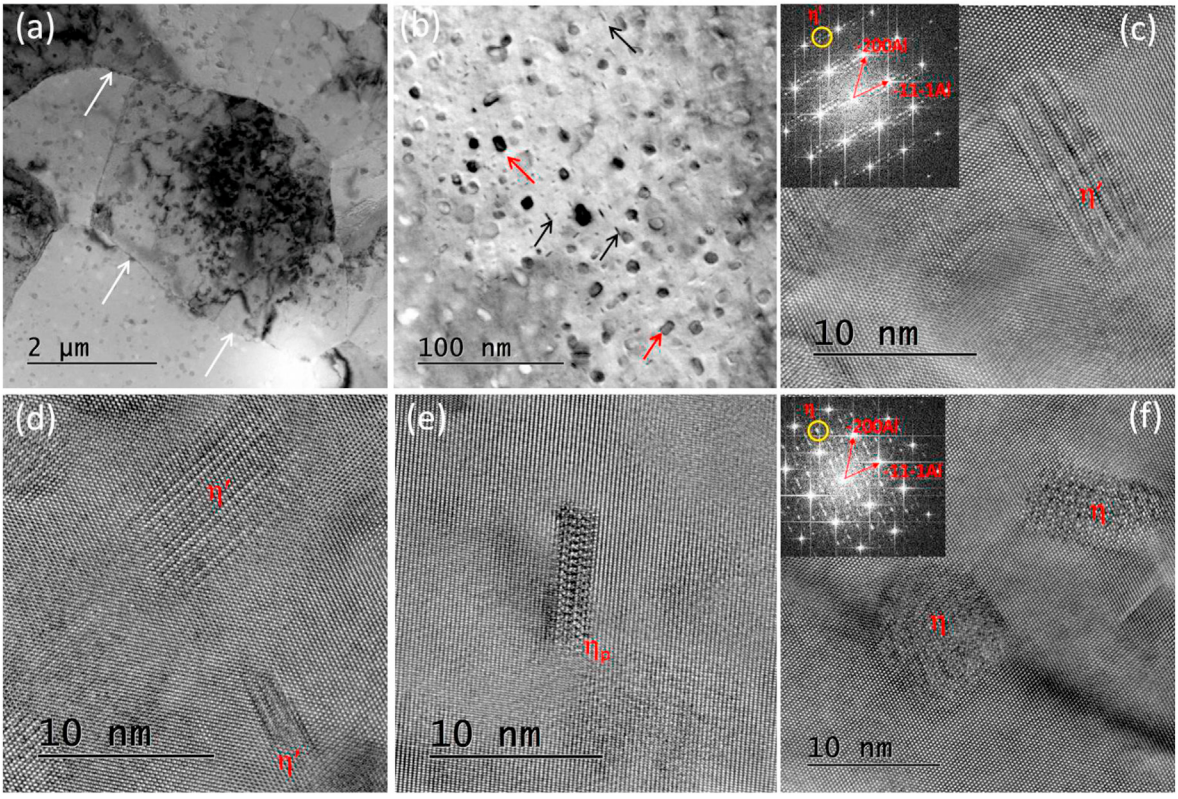

Fig. 8. TEM (a,b) and HRTEM (c–f) images of the ECAPed 7075 Al heated up to 270 °C viewed along a $<110>_{Al}$ direction. Precipitates at GBs were pointed out by white arrows in (a), the disk like η_p and η' metastable phases were pointed out by black arrows, and rod like η stable phase was pointed out by red arrows in (b). (c,d) HRTEM images of η' metastable phase and its Fourier transformation pattern. (e) HRTEM image of η_p metastable phase viewed along a $<112>_{Al}$ direction. (f) HRTEM image of η stable phase and the inset shows the Fourier transformation pattern. (For interpretation of the references to colour in this figure legend, the reader is referred to the Web version of this article.)

The as-ECAPed sample has the yield strength of 350 MPa and tensile ductility of 19.2%. Heating up to 190 °C slightly lowered both yield strength and ductility to 330 MPa and 17.4%, respectively, and heating up to 270 °C enhanced the yield strength up to 380 MPa by sacrificing the tensile ductility (10.8%). Final heating to 300 °C shifted the tensile curve downwards with decreased yield strength of 210 MPa and tensile ductility of 11.5%. The yield strength and tensile ductility against the heating temperature were plotted in Fig. 2(b) and (c), respectively. One can see the yield strength drops slightly down after region I (i.e. the 1st endotherm), and increases to form a hardening peak at 270 °C accompanied with a significant loss of ductility after region II (i.e., the 1st exotherm), and drops down significantly at 300 °C.

3.3. Microstructures and precipitation

3.3.1. As-ECAPed 7075 Al alloy

To provide insight into the influence of temperature on the

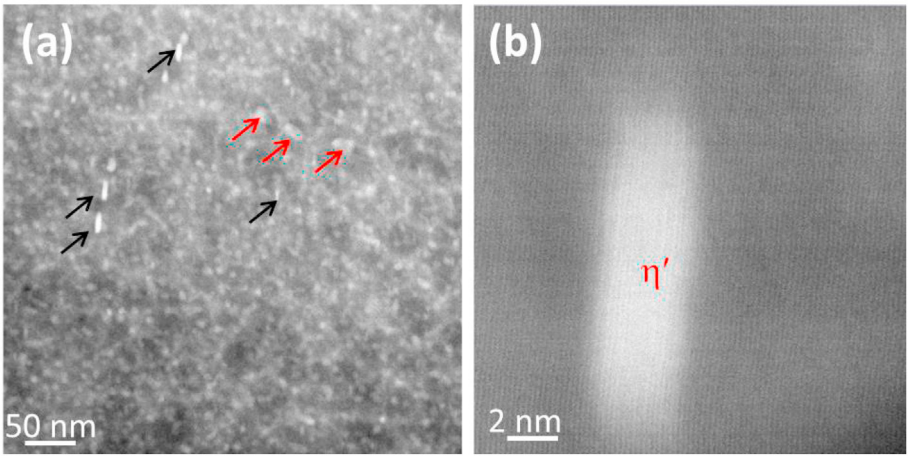

Fig. 9. The HAADF-STEM image of the ECAPed 7075 Al heated up to 270 °C viewed along a <112>$_{Al}$ direction. (a) Disk like η_p and η' metastable phases were pointed by black arrows, and rod like η stable phase was pointed by red arrows, respectively. (b) Magnified HAADF-STEM image of η' precipitate. (For interpretation of the references to colour in this figure legend, the reader is referred to the Web version of this article.)

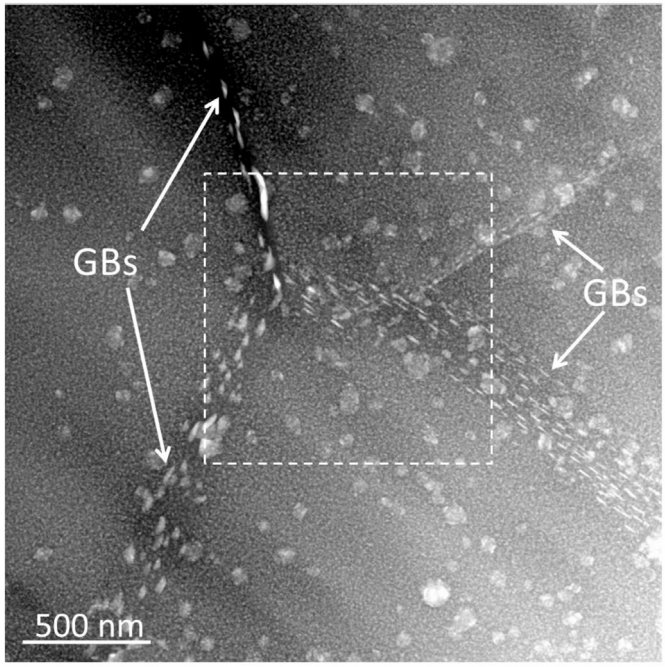

Fig. 10. The HAADF-STEM image of the ECAPed 7075 Al alloy heated up to 270 °C. Disk and rod like precipitates were lying on GBs, as pointed by white arrows. Spherical CrMn rich phases were at grain interiors.

underlying reactions and their role on mechanical behavior, microstructural analyses were carried out by using TEM. As shown in Fig. 3(a) for the TEM images of as-ECAPed 7075 Al alloy. The as-ECAPed 7075 Al alloy is composed of equiaxed grains. Statistics of the grains indicated that the grain size ranges from approximately 500 nm to 5 μm with an average grain size of about 2.1 μm, as shown in Fig. 4(a). Selected area electron diffraction (SAED) pattern of several grains marked by white circle in Fig. 3(a) revealed these grains have both high angle grain boundary (GB) of 37° and low angle GB of 7°, as shown in Fig. 3(b). These equiaxed grains were formed by dynamic recrystallization that can be attributed to the imposed large ECAP deformation strain and elevated temperature [12,13].

Spherical and cylindrical-shaped precipitates were observed most often in the grain interiors but very seldom at the GBs. These precipitates have been identified as primarily CrMn rich phase by the EDS mapping in Section 3.3.3 below. Statistic studies on these CrMn rich particles revealed that their size varies from 20 nm to 100 nm and the average size is 52 nm (Fig. 4(b)), the interparticle distance changes from 50 nm to 450 nm with an average value of 180 nm (Fig. 4(c)). The TEM results show that the dislocation density in most grains is not high, although high dislocation densities are sometimes observed, as shown in Fig. 3(c). In this case, high-density of dislocation networks are intermixed with precipitates. Careful observation discerned that some dislocations were pinned by the precipitates, as highlighted by black arrows in Fig. 3(d). Fig. 3(e and f) represent bright field TEM image and corresponding SAED pattern of as-ECAPed 7075 Al alloy. Blue and red lines were drawn to distinguish the two diffraction patterns from the two circled grains. Related calculation revealed a small misorientation angle of 8° between the two circled grains [69]. Two recrystallized grains below 1 μm were ponited by black arrows. It has been reported that UFG materials ECAPed at elevated temperatures have a higher fraction of low-angle GBs, in comparison with those processed at room temperature [70]. A possible explanation for this observation may be the kinetic recovery of dislocations into dislocation walls at higher temperatures. This suggestion is consistent with the low dislocation density observed herein, and hence only pinned dislocations remain after deformation.

Except large CrMn rich particles, HRTEM and HAADF-STEM results also found much finer GP II zones, η_p and η' metastable precipitates with sizes smaller than 10 nm, as shown in Fig. 5 viewed along a <112>$_{Al}$ direction. Since all the disc like GP II zones, η_p and η' metastable phases precipitated and lie on the $\{111\}_{Al}$ planes in the Al-matrix, one fourth of them appear edge-on as pointed by black arrows in Fig. 5(a,d), and three fourth appear about round-shape in the $[112]_{Al}$ projection. Fig. 5(b) shows the well-known coherent GP II zone consisting of a few atoms in thickness on $\{111\}_{Al}$ planes, and the less-known hexagonal-structured η_p metastable phase, or η-precursor distinguishable from the other precipitates by its lattice parameter $c = 4d_{Al<111>}$ approximately [71]. Fig. 5(c) shows the hexagonal-structured η' metastable phase distinguishable from the other precipitates by its lattice parameter $c = 6d_{Al<111>}$ approximately [72].

In the HAADF-STEM image, the Cr, Mn and Zn etc. elements with higher atomic numbers appear bright contrast, while Al and Mg elements with lower atomic numbers appear dark contrast. The

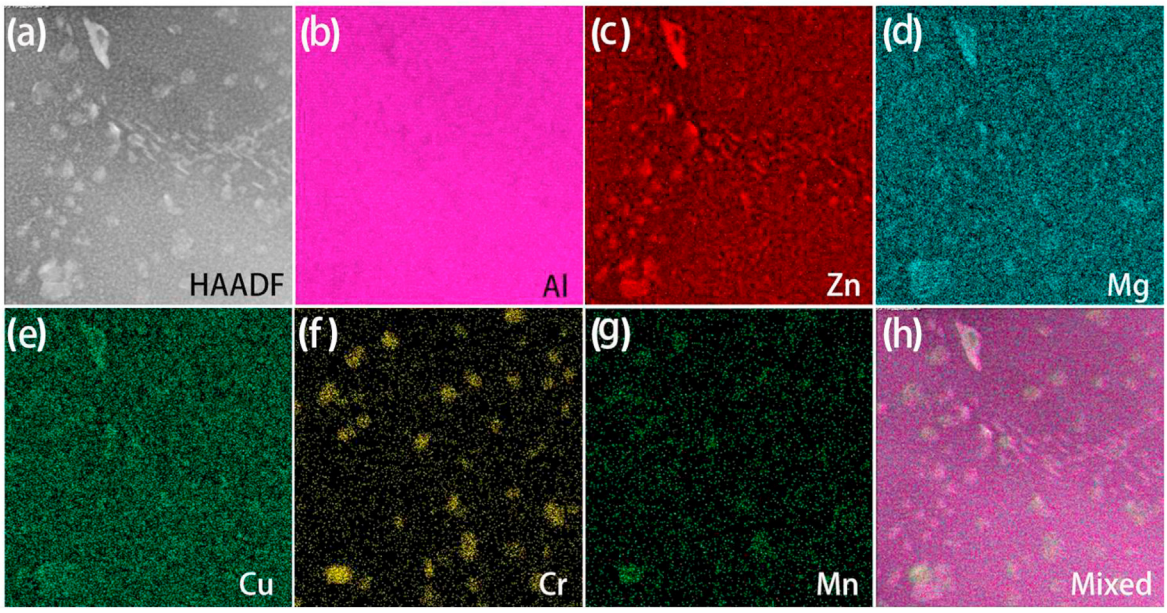

Fig. 11. EDS Al, Zn, Cu, Cr and Mn mapping images of the ECAPed 7075 Al alloy heated up to 270 °C. The mapping area was framed in Fig. 9 by dashed white rectangular.

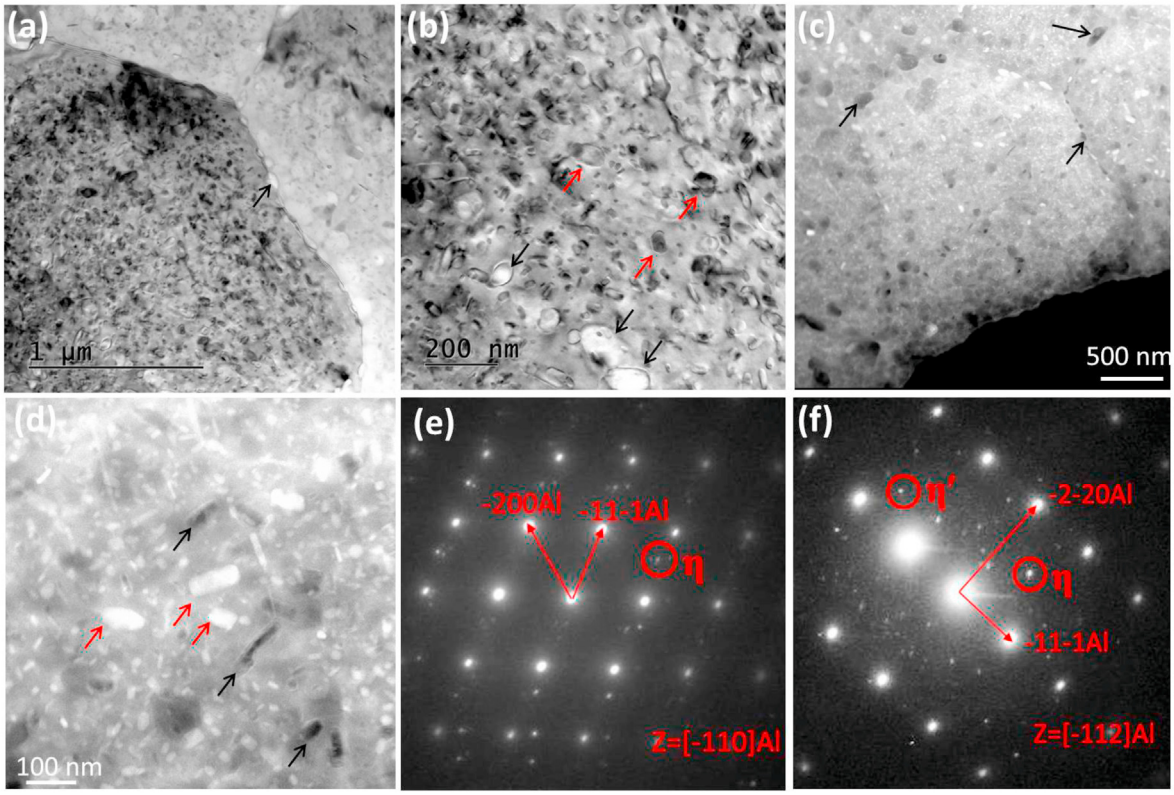

Fig. 12. Bright field TEM (a,b) and HAADF-STEM (c,d) images as well as SAED patterns of the ECAPed 7075 Al alloy heated up to 300 °C. The white precipitates marked by black arrows in (a) and (b) were caused by their peeling off the surface of TEM specimen, and the same case for the black precipitates pointed by black arrows in (c) and (d). (e) and (f) are SAED patterns from $[-110]_{Al}$ and $[-112]_{Al}$ directions from which η and η′ exist in the sample.

bright GP II zones, η_p and η′ metastable phases are Zn-rich and also contain Mg and Al atoms, their detailed structures and compositions were determined by atom-resolution imaging and quantitative image simulation analysis [54,55]. In Fig. 5(d), the CrMn rich particle was pointed by red arrow (will be characterized by EDS below), and the Zn rich precipitates on the surface of CrMn rich particle was pointed by blue arrow. Fig. 5(e) shows the HAADF-STEM image of a η_p phase. Based on Refs 54 and 55, η_p phase possesses at least 11-atomic-layers in the $\{111\}_{Al}$ planes, and Zn atoms can be distinguished clearly due to its specific atomic

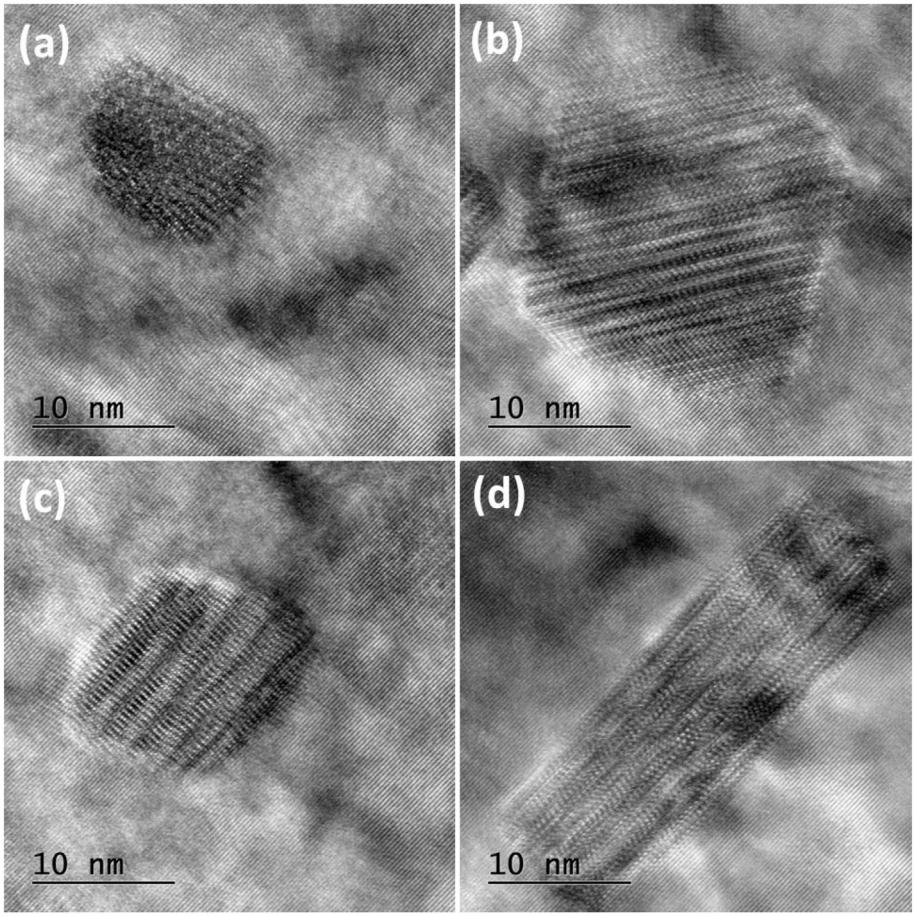

Fig. 13. HRTEM images of stable η phase which have various orientation relationships with Al matrix. (a) $(0001)\eta_4//(110)_{Al}$, $[1\bar{2}10]\ \eta_4//[\bar{1}11]_{Al}$; (b) $(0001)\eta_{12}//(\bar{1}13)_{Al}$, $[\bar{1}120]\ \eta_{12}//[\bar{1}10]_{Al}$; (c) $(0001)\eta_3//(\bar{1}11)_{Al}$, $[\bar{1}120]\eta_3//[\bar{1}10]_{Al}$; (d) $(0001)\eta_2//(\bar{1}11)_{Al}$, $[10\bar{1}0]\ \eta_2//[\bar{1}10]_{Al}$.

position viewed along a $<112>_{Al}$ direction, while the Zn atoms in η′ metastable phase is hard to be distinguished one by one, as shown in Fig. 5(d). The HAADF-STEM images further confirmed η_p and η′ metastable precipitates with different lattice parameters of *c*.

3.3.2. ECAPed 7075 Al alloy heated up to 190 °C

Increasing the temperature to 190 °C did not have an obvious influence on the microstructures of Al matrix (grain size and its distribution) or CrMn rich particle (density and morphology), but dissolved GP zones, η_p and η′ metastable phases. Only a few grains were observed to have a high density of dislocations, as shown in Fig. 6(a). Fig. 6(b) represents a dark-field TEM image showing a dislocation network pinned by precipitates. Moreover, the HAADF-STEM image of the ECAPed 7075 Al heated up to 190 °C viewed along a $<112>_{Al}$ direction did not observe the traces of GP zones, η_p or η′ metastable phases (Fig. 7), suggesting that they dissoluted when heating up to 190 °C.

3.3.3. ECAPed 7075 Al alloy heated up to 270 °C

As shown in Figs. 8–11, increasing the temperature to 270 °C did not change the grain size or distribution of the UFG Al matrix, but significantly reduced the dislocation density. During heating, there precipitated high densities of GP zones, η_p and η′ metastable phases both at GBs (Figs. 8(a) and 10) and grain interiors (Fig. 8(b-e) and Fig. 9(a)). Moreover, there exists large amount of rod like η stable phase both at GBs (Fig. 10) and grain interiors (Fig. 8(b,f) and Fig. 9(a)) which were transformed from η_p and η′ metastable phases.

As shown in Fig. 8(b) viewed along a $<110>_{Al}$ direction, high density of rod like η stable phase with sizes of about 10 nm was discerned, as pointed by red arrows. HRTEM and corresponding Fourier transformation pattern in Fig. 8(e) confirmed the hexagonal Laves $MgZn_2$ phase. Moreover, HRTEM image and corresponding Fourier transformation pattern in Fig. 8(c and d) as well as magnified HAADF-STEM image in Fig. 9(b) confirmed the existence of hexagonal η′ metastable phase. HRTEM image in Fig. 8(e) provides the evidence of hexagonal-structured η_p metastable phase identified from the other precipitates by $c = 4d_{Al<111>}$ approximately [71].

Fig. 10 shows the low magnification HAADF-STEM image scanned at two triple GB junctions. High density of disk like η_p and η′ metastable precipitates with sizes of several tens of nanometer can be seen on the GB at the lower right corner. This GB was projected as a band with a certain width but not a line because it was inclined along electron beam. High density of rod like η stable phase with even larger size (some approach 100 nm) was also found on the GB at the lower left corner which was also projected as a band shape due to its inclination to electron beam. EDS mapping images of Al, Zn, Cu, Cr and Mn further confirmed the above analysis. The precipitates on GBs are rich of Zn and Mg, and those at grain interiors are rich of Cr and Mn.

3.3.4. ECAPed 7075 Al alloy heated up to 300 °C

Increasing the temperature up to 300 °C did not alter the grain

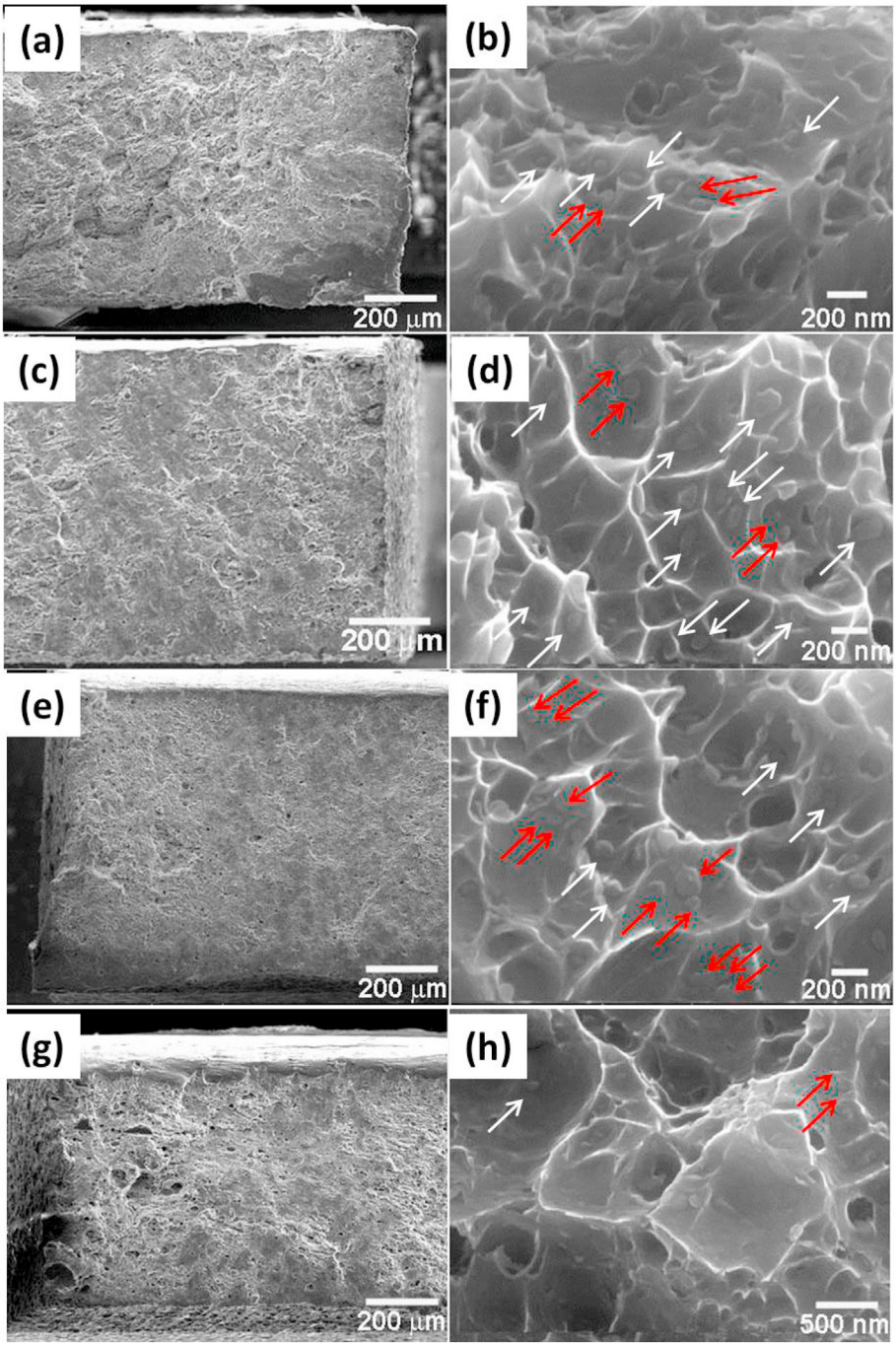

Fig. 14. SEM images of the fracture surfaces of as-ECAPed 7075 Al alloys (a,b), the UFG 7075 Al alloy heated up to 190 °C (c,d), 270 °C (e,f) and 300 °C (g,h), respectively. (a,c,e,g) lower magnification, (b,d,f,h) higher magnification. One precipitate existed at one dimple bottom was pointed by white arrows, and two or three precipitates coexisted at one dimple bottom were pointed by red arrows. (For interpretation of the references to colour in this figure legend, the reader is referred to the Web version of this article.)

size or distribution, but led to transformation of metastable η_p and η' to η precipitate, and coarsening of the η precipitate at the GBs and within the grains, as shown in Figs. 12 and 13. The coarsened η precipitate approaches 100 nm, as shown in Fig. 12(b,d). SAED patterns from $[-110]_{Al}$ and $[-112]_{Al}$ directions in Fig. 12(e and f) verified that η' still exists in the sample except stable η phase. Fig. 13 shows HRTEM images of stable η phase which have various orientation relationships with Al matrix [73,74].

3.4. Deformation and fracture morphologies

To further understand the tensile behavior and establish the relationship between microstructures and mechanical properties, we studied the fracture mode and surface morphology using the SEM. Fig. 14 shows SEM images of the macro- and micro-scale fracture surfaces of as-ECAPed 7075 Al alloy and the corresponding samples heated up to 190, 270 and 300 °C with a heating rate of 20 °C/min, respectively. From the macro-scale SEM images

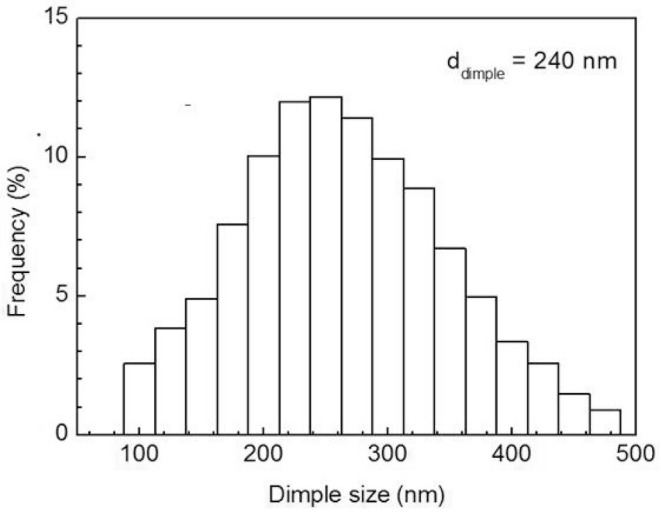

Fig. 15. Histogram of the dimple size in the fracture surface of as-ECAPed 7075 Al alloy, d_{dimple} represents the average value.

(Fig. 14a,c,e,g), the fracture surface of the as-ECAPed 7075 Al alloy is irregular, with a high concentration of uneven concave and protrusion. Increasing the temperature to 270 °C resulted in the formation of interdispersed macroscopically smooth regions (e.g., low plasticity), which is consistent with the aforementioned decrease in ductility during annealing. From Fig. 14(b,d,f,h), it is evident that the material fractured in a ductile manner, as evidenced by the homogeneously distributed honeycomb-like dimples.

Careful statistics showed that the dimple size ranged from about 100 nm to 500 nm in the case of the as-ECAPed (Fig. 15) and 190 °C annealed materials. The average dimple size is 240 nm, which is slightly larger than the average interpartcile distance of the CrMn rich phase (180 nm in Fig. 4(c)) as determined on the basis of TEM results. Moreover, spherical particles pointed by arrows are observed at the bottom of the dimples, which have a similar size and morphology as the CrMn rich phase observed via TEM. These results suggest that during tension, the CrMn rich phase resists deformation and detaches from the matrix. For the as-ECAPed 7075 Al alloy and that heated up to 190 °C, one precipitate often existed at one dimple bottom, as pointed by white arrows in Fig. 14(b,d), while two or three precipitates occasionally coexisted at one dimple bottom as pointed by red arrows in Fig. 14(b,d). This explains why the average dimple size is lightly larger than the average interpartcile distance of the CrMn rich phase.

After increasing the temperature to 270 and 300 °C, the range of dimple sizes increased to 100−1000 nm but dimple geometry was shallow particularly in the case of the material heated to 300 °C (Fig. 14(h)). Moreover, multiple CrMn rich particles were frequently noted to occupy the same dimple in the 270 °C heated sample (Fig. 14(f)) a phenomena that was occasionally observed for the as-ECAPed and 190 °C heated samples. On the basis of TEM results, the presence of a network of discontinuous brittle η and η′ phases along the GBs significantly impairs the deformation ability of the GBs. Therefore, during tensile loading, micropores can be also formed at the interfaces of the η and η′ phases at the GBs, and eventually grow into grain interiors by trapping several CrMn rich particles in one dimple. Hence, despite the presence of a high density of transgranular precipitates, the type, distribution and morphology of GB precipitates also affected fracture processes in the ECAPed 7075 alloys heated up to 270 and 300 °C.

Fig. 16 shows the macro- and micro-scale fracture morphologies of the 7075 Al alloys subjected to different heating temperatures. All samples failed with a shear fracture mode with a corresponding shear fracture angle (the angle between the fracture surface and tension axis) of approximately 75° for the as-ECAPed and 190 °C heated samples and 80° for the 270 °C and 300 °C heated samples. The shear fracture is attributable to the nanostructures which resulted in a decreased ratio of the average critical normal fracture stress to shear fracture stress [75,76]. Careful observation on the sample surface revealed numerous localized plastic deformation

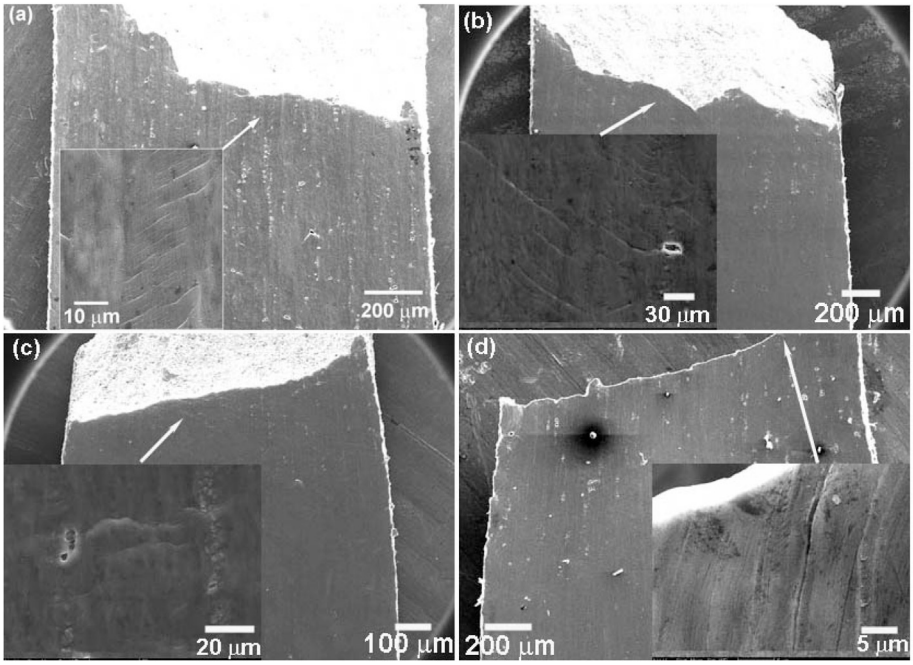

Fig. 16. SEM images from face-view of the as-ECAPed 7075 Al (a) and the UFG 7075 Al alloys heated up to 190 (b), 270 (c) and 300 °C (d) to show shear fracture and micro shear bands.

markings or traces parallel with each other near the fracture edge within the necking zones of the as-ECAPed and 190 °C heated samples. Several published studies reported similar deformation traces in UFG Al [77,78], Al6082 alloys [79], Ni [80], and Cu [80], and these were described as microscopic or mesoscopic shear bands or shear planes. The distances between shear bands vary from several micrometers to several tens of micrometers, and the lengths of the shear bands extend from several micrometers to several hundreds of micrometers. The shear bands are much coarser in the 270 °C and 300 °C heated samples, as shown in Fig. 16(c and d). This result suggests that the formation of the high density of fine shear bands may have enhanced the plastic deformation capability and overall tensile ductility.

4. Conclusions

In this study, an age-hardened 7075 Al alloy was ECAP processed at an elevated temperature (i.e., 250 °C). Prior to ECAP processing, the 7075 Al alloy was first homogenized to form super saturated solid solution. Study of the evolution of microstructure and tensile response during annealing at various temperatures led to the following findings:

1. Upon annealing, three sequential phase transitions occurred: first, dissolution reactions of GP zones, metastable η_p and η', second, precipitations of GP zones, metastable η' and η_p/stable η phases and third, subsequent η transformation of the metastable η' and η_p, stable η phase coarsening. The grain size of the Al matrix was stable up to 300 °C.
2. The dissolution reactions of GP zones, metastable η_p and η' correspond to a slight decrease in strength and ductility.
3. The precipitations of the GP zones, metastable η' and η_p/stable η phases result in an increase in strength with significant decrease in ductility which was caused by grain boundary precipitation of the metastable η' and η_p/stable η phases.
4. The η transformation of the metastable η' and η_p, and subsequent coarsening stable η phases correspond to a dramatic drop in yield strength.

CRediT authorship contribution statement

Yonghao Zhao: Conceptualization, Methodology, Investigation, Data curation. **Jizi Liu:** Methodology, Investigation, Data curation. **Troy D. Topping:** Methodology, Investigation. **Enrique J. Lavernia:** Supervision, Writing - review & editing, Funding acquisition.

Declaration of competing interest

The authors declare that they have no known competing financial interests or personal relationships that could have appeared to influence the work reported in this paper.

Acknowledgements

Y.H. Zhao acknowledges financial supports from the Fundamental Research Funds for the Central Universities (Grant No. 30919011405), the National Natural Science Foundation of China (Grant No. 51971112 and 51225102) and National Key R&D Program of China (Grant No. 2017YFA0204403).

References

[1] Y. Cao, S. Ni, X.Z. Liao, et al., Structural evolutions of metallic materials processed by severe plastic deformation, Mater. Sci. Eng. R Rep. 133 (2018) 1–59.
[2] I.A. Ovid'ko, R.Z. Valiev, Y.T. Zhu, Review on superior strength and enhanced ductility of metallic nanomaterials, Prog. Mater. Sci. 94 (2018) 462–540.
[3] C.C. Koch, D.G. Morris, K. Lu, A. Inoue, Ductility of nanostructured materials, MRS Bull. 24 (1999) 54–58.
[4] C.C. Koch, Optimization of strength and ductility in nanocrystalline and ultrafine grained metals, Scripta Mater. 49 (2003) 657–662.
[5] E. Ma, Instabilities and ductility of nanocrystalline and ultrafine-grained metals, Scripta Mater. 49 (2003) 663–668.
[6] C.C. Koch, K.M. Youssef, R.O. Scattergood, K.L. Murty, Breakthroughs in optimization of mechanical properties of nanostructured metals and alloys, Adv. Eng. Mater. 7 (2005) 787–794.
[7] E. Ma, Eight routes to improve the tensile ductility of bulk nanostructured metals and alloys, JOM 58 (2006) 49–53.
[8] Y.H. Zhao, Y.T. Zhu, E.J. Lavernia, Strategies for improving tensile ductility of bulk nanostructured materials, Adv. Eng. Mater. 12 (2010) 769–778.
[9] C.C. Koch, R.O. Scattergood, K.A. Darling, J.E. Semones, Stabilization of nanocrystalline grain size by solute additions, J. Mater. Sci. 43 (2008) 7264–7272.
[10] K. Zhang, J.R. Weertman, J.A. Eastman, Rapid stress-driven grain coarsening in nanocrystalline Cu at ambient and cryogenic temperatures, Appl. Phys. Lett. 87 (2005), 061921.
[11] R.Z. Valiev, R.K. Isamgaliev, I.V. Alexandrov, Bulk nanostructured materials from severe plastic deformation, Prog. Mater. Sci. 45 (2000) 103–189.
[12] R.Z. Valiev, T.G. Langdon, Principles of equal-channel angular pressing as a processing tool for grain refinement, Prog. Mater. Sci. 51 (2006) 881–981.
[13] I.J. Beyerlein, L.S. Toth, Texture evolution in equal-channel angular extrusion, Prog. Mater. Sci. 54 (2009) 427–510.
[14] C.Y. Yu, P.L. Sun, P.W. Kao, C.P. Chang, Mechanical properties of submicron-grained aluminum, Scripta Mater. 52 (2005) 359–363.
[15] C. Xu, K.N. Xia, T.G. Langdon, The role of back pressure in the processing of pure aluminum by equal-channel angular pressing, Acta Mater. 55 (2007) 2351–2360.
[16] S.O. Gashti a, A. Fattah-alhosseini a, Y. Mazaheri a, M.K. Keshavarz, Microstructure, mechanical properties and electrochemical behavior of AA1050 processed by accumulative roll bonding (ARB), J. Alloys Compounds, J. Alloys Compd. 688 (2016) 44–55.
[17] F.H. Dalla Torre, A.A. Gazder, E.V. Pereloma, C.H.J. Davies, Recent progress on the study of the microstructure and mechanical properties of ECAE copper, J. Mater. Sci. 42 (2007) 9097–9111.
[18] Y.H. Zhao, Y. Li, T.D. Topping, X.Z. Liao, Y.T. Zhu, R.Z. Valiev, E.J. Lavernia, Ductility of ultrafine-grained copper processed by equal-channel angular pressing, Int. J. Mater. Res. 100 (2009) 1647–1652.
[19] Y.H. Zhao, T. Topping, Y. Li, E. J Lavernia, Strength and ductility of bi-modal Cu, Adv. Eng. Mater. 13 (2011) 865–871.
[20] J. Wang, Y. Iwahashi, Z. Horita, M. Furukawa, M. Nemoto, R.Z. Valiev, T.G. Langdon, An investigation of microstructural stability in an Al-Mg alloy with submicrometer grain size, Acta Mater. 44 (1996) 2973–2982.
[21] J. May, M. Dinkel, D. Amberger, H.W. Hoppel, M. Goken, Dislocation density and grain structure of ultrafine-grained aluminum and aluminum-magnesium alloys, Metall. Mater. Trans. 38 (2007) 1941–1945.
[22] Y.H. Zhao, X.Z. Liao, Z. Horita, T.G. Langdon, Y.T. Zhu, Determining the optimal stacking fault energy for achieving high ductility in ultrafine-grained Cu-Zn alloys, Mater. Sci. Eng., A 493 (2008) 123–129.
[23] Y.H. Zhao, X.Z. Liao, Y.T. Zhu, Z. Horita, T.G. Langdon, Influence of stacking fault energy on nanostructure formation under high pressure torsion, Mater. Sci. Eng., A 410 (2005) 188–193.
[24] C. Xu, M. Furukawa, Z. Horita, T.G. Langdon, Using ECAP to achieve grain refinement, precipitate fragmentation and high strain rate superplasticity in a spray-cast aluminum alloy, Acta Mater. 51 (2003) 6139–6149.
[25] C. Xu, M. Furukawa, Z. Horita, T.G. Langdon, Influence of ECAP on precipitate distributions in a spray-cast aluminum alloy, Acta Mater. 53 (2005) 749–758.
[26] Y.H. Zhao, X.Z. Liao, Z. Jin, R.Z. Valiev, Y.T. Zhu, Microstructures and mechanical properties of ultrafine grained 7075 Al alloy processed by ECAP and their evolutions during annealing, Acta Mater. 52 (2004) 4589–4599.
[27] Y.H. Zhao, X.Z. Liao, Y.T. Zhu, R.Z. Valiev, Enhanced mechanical properties in ultrafine grained 7075 Al alloy, J. Mater. Res. 20 (2005) 288–291.
[28] J. Gubicza, I. Schiller, N.Q. Chinh, J. Illy, Z. Horita, T.G. Langdon, The effect of severe plastic deformation on precipitation in supersaturated Al-Zn-Mg alloys, Mater. Sci. Eng., A 460 (2007) 77–85.
[29] G. Sha, Y.B. Wang, X.Z. liao, Z.C. Duan, S.P. Ringer, T.G. Langdon, Influence of equal-channel angular pressing on precipitation in an Al-Zn-Mg-Cu alloy, Acta Mater. 57 (2009) 3123–3132.
[30] Z.C. Duan, N.Q. Chinh, C. Xu, T.G. Langdon, Developing processing routes for the equal-channel angular pressing of age-hardenable aluminum alloys, Metall. Mater. Trans. 41 (2010) 802–809.
[31] M. Samaee, S. Najafi, A.R. Eivani, H.R. Jafarian, J. Zhou, Simultaneous improvements of the strength and ductility of fine-grained AA6063 alloy with increasing number of ECAP passes, Mater. Sci. Eng., A 669 (2016) 44–55.
[32] M. Bahrami, N. Helmi, K. Dehghani, M.K.B. Givi, Exploring the effects of SiC reinforcement incorporation on mechanical properties of friction stir welded 7075 aluminum alloy: fatigue life, impact energy, tensile strength, Mater. Sci. Eng., A 595 (2014) 173–178.
[33] T. Hu, K. Ma, T.D. Topping, J.M. Schoenung, E.J. Lavernia, Precipitation phenomena in an ultrafine-grained Al alloy, Acta Mater. 61 (2013) 2163–2178.
[34] P.V. Liddicoat, X.Z. Liao, Y.H. Zhao, Y.T. Zhu, M.Y. Murashkin, E.J. Lavernia, R.Z. Ruslan, S.P. Ringer, Nanostructural hierarchy increases the strength of

aluminium alloys, Nat. Commun. 1 (2010) 63.
[35] R. Flores-Campos, I. Estrada-Guel, M. Miki-Yoshida, R. Martínez-Sánchez, J.M. Herrera-Ramírez, Microstructure and mechanical properties of 7075 aluminum alloy nanostructured composites processed by mechanical milling and indirect hot extrusion, Mater. Char. 63 (2012) 39–46.
[36] K. Ma, H. Wen, T. Hu, T.D. Topping, D. Isheim, D.N. Seidman, E.J. Lavernia, J.M. Schoenung, Mechanical behavior and strengthening mechanisms in ultrafine grain precipitation-strengthened aluminum alloy, Acta Mater. 62 (2014) 141–155.
[37] Y. Duan, L. Tang, G. Xu, Y. Deng, Z. Yin, Microstructure and mechanical properties of 7005 aluminum alloy processed by room temperature ECAP and subsequent annealing, J. Alloys Compd. 664 (2016) 518–529.
[38] M.H. Shaeri, M. Shaeri, M. Ebrahimi, M.T. Salehi, S. H Seyyedein, Effect of ECAP temperature on microstructure and mechanical properties of Al-Zn-Mg-Cu alloy, Prog. Nat. Sci. 26 (2016) 182–191.
[39] A. Orozco-Caballero, P. Hidalgo-Manrique, C.M. Cepeda-Jiménez, P. Rey, D. Verdera, O.A. Ruano, F. Carreño, Strategy for severe friction stir processing to obtain acute grain refinement of an Al-Zn-Mg-Cu alloy in three initial precipitation states, Mater. Char. 112 (2016) 197–205.
[40] K. Ma, T. Hu, H. Yang, T. Topping, A. Yousefiani, E.J. Lavernia, J.M. Schoenung, Coupling of dislocations and precipitates: impact on the mechanical behavior of ultrafine grained Al-Zn-Mg alloys, Acta Mater. 103 (2016) 153–164.
[41] S. Sabbaghianrad, T.G. Langdon, An evaluation of the saturation hardness in an ultrafine-grained aluminum 7075 alloy processed using different techniques, J. Mater. Sci. 50 (2015) 4357–4365.
[42] M.H. Li, Y.Q. Yang, Z.Q. Feng, G.H. Feng, B. Huang, Y.X. Chen, M. Han, J.G. Ru, Influence of equal-channel angular pressing on aging precipitation in 7050 Al alloy, Intermetallics 55 (2014) 49–55.
[43] W. Huo, L. Hou, H. Cui, L. Zhuang, J. Zhang, Fine-grained AA 7075 processed by different thermo-mechanical processings, Mater. Sci. Eng., A 618 (2014) 244–253.
[44] T. Hu, K. Ma, T.D. Topping, B. Saller, A. Yousefiani, J.M. Schoenung, E.J. Lavernia, Improving the tensile ductility and uniform elongation of high-strength ultrafine-grained Al alloys by lowering the grain boundary misorientation angle, Scripta Mater. 78 (2014) 25–28.
[45] M.H. Shaeri, M.T. Salehi, S.H. Seyyedein, M.R. Abutalebi, J.K. Park, Microstructure and mechanical properties of Al-7075 alloy processed by equal channel angular pressing combined with aging treatment, Mater. Des. 57 (2014) 250–257.
[46] A. Deschamps, F. De Geuser, Z. Horita, S. Lee, G. Renou, Precipitation kinetics in a severely plastically deformed 7075 aluminium alloy, Acta Mater. 66 (2014) 105–117.
[47] M. Gazizov, R. Kaibyshev, The precipitation behavior of an Al-Cu-Mg-Ag alloy under ECAP, Mater. Sci. Eng., A 588 (2013) 65–75.
[48] A.D. Isadare, B. Aremo, M.O. Adeoye, O.J. Olawale, M.D. Shittu, Effect of heat treatment on some mechanical properties of 7075 aluminium alloy, Mater. Res. 16 (2012) 190–194.
[49] K.G. Krishna, K. Sivaprasad, K. Venkateswarlu, K.C.H. Kumar, Microstructural evolution and aging behavior of cryorolled Al-4Zn-2Mg alloy, Mater. Sci. Eng., A 535 (2012) 129–135.
[50] S.R. Kumar, K. Gudimetla, P. Venkatachalam, B. Ravisankar, K. Jayasankar, Microstructural and mechanical properties of Al 7075 alloy processed by equal channel angular pressing, Mater. Sci. Eng., A 533 (2012) 50–54.
[51] K.R. Cardoso, D.N. Travessa, W.J. Botta, A.M. Jorge Jr., High Strength AA7050 Al alloy processed by ECAP: microstructure and mechanical properties, Mater. Sci. Eng., A 528 (2011) 5804–5811.
[52] H. Löffler, I. Kovács, J. Lendvai, Decomposition processes in Al-Zn-Mg alloys, J. Mater. Sci. 18 (1983) 2215–2240.
[53] J. Lendvai, Precipitation and strengthening in aluminium alloys, Mater. Sci. Forum 217–222 (1996) 43–56.
[54] J.Z. Liu, J.H. Chen, D.W. Yuan, C.L. Wu, J. Zhu, Z.Y. Sheng, Fine precipitation scenarios of AlZnMg(Cu) alloys revealed by advanced atomic-resolution electron microscopy study Part I: structure determination of the precipitates in AlZnMg(Cu) alloys, Mater. Char. 99 (2015) 277–286.
[55] J.Z. Liu, J.H. Chen, Z.R. Liu, C.L. Wu, Fine precipitation scenarios of AlZnMg(Cu) alloys revealed by advanced atomic-resolution electron microscopy study Part II: fine precipitation scenarios in AlZnMg(Cu) alloys, Mater. Char. 99 (2015) 142–149.
[56] K. Stiller, P.J. Warren, V. Hansen, J. Angenete, J. Gjφnnes, Investigation of precipitation in an Al-Zn-Mg alloy after two-step ageing treatment at 100 degrees and 150 degrees C, Mater. Sci. Eng. A270 (1999) 55–63.
[57] L.K. Berg, J. Gjφnnes, V. Hansen, X.Z. Li, M.K. Wedel, G. Waterloo, D. Schryvers, L.R. Wallenberg, GP-zones in Al-Zn-Mg alloys and their role in artificial aging, Acta Mater. 49 (2001) 3443–3451.
[58] T. Engdahl, V. hasen, P.J. Warren, K. Stiller, Investigation of fine scale precipitates in Al-Zn-Mg alloys after various heat treatments, Mater. Sci. Eng., A 327 (2002) 59–64.
[59] J. Gjφnnes, C.J. Simensen, An electron microscope investigation of the microstructure in an aluminium-zinc-magnesium alloy, Acta Mater. 18 (1970) 881–890.
[60] Y. Komura, K. Tokunaga, Structural studies of stacking variants in Mg-base Friauf-Laves phases, Acta Crystallogr. B 36 (1980) 1548–1554.
[61] S.L. Semiatin, D.P. Delo, V.M. Segal, R.E. Goforth, N.D. Frey, Workability of commercial-purity titanium and 4340 steel during equal channel angular extrusion at cold-working temperatures, Metall. Mater. Trans. 30 (1999) 1425–1435.
[62] A. Yamashita, D. Yamaguchi, Z. Horita, T.G. Langdon, Influence of pressing temperature on microstructural development in equal-channel angular pressing, Mater. Sci. Eng., A 287 (2000) 100–106.
[63] Y.H. Zhao, X.Z. Liao, S. Cheng, E. Ma, Y.T. Zhu, Simultaneously increasing the ductility and strength of nanostructured alloys, Adv. Mater. 18 (2006) 2280–2283.
[64] E.J. Kirkland, R.F. Loane, J. Silcox, Simulation of angular dark field stem images using a modified multiscale method, Ultramicroscopy 23 (1987) 77–96.
[65] X.J. Jiang, B. Boble, B. Holme, G. Waterloo, J. Tafto, Differential scanning calorimetry and electron diffraction investigation on low-temperature aging in Al-Zn-Mg alloys, Metall. Mater. Trans. 31 A (2000) 339–348.
[66] R. Deiasi, P.N. Adler, Calorimetric studies of 7000 series aluminum alloys: I. Matrix precipitate characterization of 7075, Metall. Mater. Trans. 8 (1977) 1177–1183.
[67] P.N. Adler, R. Deiasi, Calorimetric studies of 7000 series aluminum alloys: II. Comparison of 7075, 7050 and RX720 alloys, Metall. Mater. Trans. 8 (1977) 1185–1190.
[68] J.M. Papazian, Calorimetric studies of precipitation and dissolution kinetics in aluminum alloys 2219 and 7075, Metall. Trans. A 13 (1982) 761–769.
[69] Z.G. Yan, Y.J. Lin, Rapid and Precise Method for Measuring Misorientation of Low Angle Grain Boundaries by Means of Transmission Electron Microscopy, 2017. China Patent, CN 106802306 A.
[70] H. Wen, Y.H. Zhao, Z. Zhang, O. Ertorer, S. Dong, E.J. Lavernia, Mechanical properties of UFG Cu by ECAP at different T, Adv. Eng. Mater. 14 (2012) 185–194.
[71] J.Z. Liu, J.H. Chen, X.B. Yang, S. Ren, C.L. Wu, H.Y. Xu, J. Zou, Revisiting the precipitation sequence in Al-Zn-Mg-based alloys bu high-resolution transmission electron microscopy, Scripta Mater. 63 (2010) 1061–1064.
[72] X.Z. Li, V. Hansen, J. Gjonnes, L.R. Wallenberg, HREM study and structure modelling of the eta' phase, the hardening precipitates in commercial Al-Zn-Mg alloys, Acta Mater. 47 (1999) 43–56.
[73] T.-F. Chung, Y.-L. Yang, M. Shiojiri, C.-N. Hsiao, W.-C. Li, C.-S. Tsao, Z. Shi, J. Lin, J.-R. Yang, An atomic scale structural investigation of nanometre-sized η precipitates in the 7050 aluminium alloy, Acta Mater. 174 (2019) 351–368.
[74] A. Bendo, K. Matsuda, A. Lervik, T. Tsuru, K. Nishimura, N. Nunomura, R. Holmestad, C.D. Marioara, K. Shimizu, H. Toda, An unreported precipitate orientation relationship in Al-Zn-Mg based allots, Mater. Char. 158 (2019), 109958.
[75] Z.F. Zhang, G. He, J. Eckert, L. Schultz, Fracture mechanisms in bulk metallic glassy materials, Phys. Rev. Lett. 91 (2003), 045505.
[76] Z.F. Zhang, J. Eckert, Unified tensile fracture criterion, Phys. Rev. Lett. 94 (2005), 094301.
[77] Y. Huang, T.G. Langdon, Using atomic force microscopy to evaluate the development of mesoscopic shear planes in materials processed by severe plastic deformation, Mater. Sci. Eng., A 358 (2003) 114–121.
[78] N.Q. Chinh, P. Szommer, Z. Horita, T.G. Langdon, Experimental evidence for grain-boundary sliding in ultrafine-grained aluminum processed by severe plastic deformation, Adv. Mater. 18 (2006) 34–39.
[79] I. Sabirov, Y. Estrin, M.R. Barnett, I. Timokhina, P.D. Hodgson, Tensile deformation of an ultrafine-grained aluminium alloy: micro shear banding and grain boundary sliding, Acta Mater. 56 (2008) 2223–2230.
[80] A. Vinogradov, S. Hashimoto, V. Patlan, K. Kitagawa, Atomic force microscopic study on surface morphology of ultra-fine grained materials after tensile testing, Mater. Sci. Eng., A 319–323 (2001) 862–866.